

7N-26-TM  
004032

THE EFFECTS OF EXTRUSION PARAMETERS ON RECRYSTALLIZATION  
KINETICS, TEXTURE, AND CORRESPONDING FRACTURE TOUGHNESS OF NiAl

T.R. Bieler, R.D. Noebe\*, M. Hebsur\*, R. Saminathan

Department of Materials Science and Mechanics  
Michigan State University, East Lansing, MI 48824-1226

\*NASA Lewis Research Center, MS 49-3, Cleveland, OH 44135

Abstract

A systematic study of extrusion textures and microstructures in stoichiometric NiAl was conducted to determine the effects that extrusion conditions have on mechanical properties. Extrusions of powder were made in steel cans at a 16:1 ratio between 1200 and 1500 K. The grain size increased with extrusion temperature from about 5  $\mu\text{m}$  to 25  $\mu\text{m}$ , and extrusion textures exhibited changes from  $\langle 110 \rangle$  to  $\langle 111 \rangle$  fiber textures. These components of texture arise from slip in the usual  $\langle 100 \rangle$  directions, with secondary slip in  $\langle 111 \rangle$  and possibly  $\langle 110 \rangle$  directions. Slip in  $\langle 111 \rangle$  directions controlled the stability of the  $\langle 110 \rangle$  deformation texture orientation. Fracture toughness also exhibits a slight increase from 5.5 to 9  $\text{MPa}\sqrt{\text{m}}$  with increasing extrusion temperature conditions. Specimens with a larger grain size and  $\langle 111 \rangle$  texture exhibited higher toughness and residual toughness after initial fracture. The increase in toughness is attributed to a combination of extrinsic grain size toughening and the reduction in the number of grains with the  $\{110\}$  cleavage plane oriented for easy cleavage.

Acknowledgement: TRB acknowledges support from an ASEE Faculty Fellowship at NASA-Lewis, which is administered through Case Western University. Discussions with J.D. Whittenberger, S.V. Raj, and M. Nathal were appreciated.

Advances in Hot Deformation Textures and Microstructures  
Edited by J.J. Jonas, T.R. Bieler and K.J. Bowman  
The Minerals, Metals & Materials Society, 1994

## Introduction

Though polycrystalline NiAl has property advantages over superalloys, poor tensile ductility and fracture toughness below the brittle-to-ductile transition temperature (BDTT) have impeded its acceptance as a high temperature structural material (1). Other than by ductile phase toughening, which has its own disadvantages (2), both microalloying and macroalloying schemes have not been successful in overcoming these problems in polycrystalline materials (3-5). In fact, room temperature ductility is a maximum for the binary compound near stoichiometric composition since ternary alloying additions tend to decrease the already poor room temperature tensile ductility and increase the BDTT (3-6).

Because fracture is most significantly influenced by the materials' microstructure (7), an alternate approach to improve the low temperature properties of NiAl is to optimize its microstructure. Grain refinement has been proposed as one method for increasing the tensile ductility of brittle, ordered intermetallic alloys (8). However, grain refinement alone without a concomitant increase in fracture toughness does not appear to be a viable method for significantly improving the room temperature ductility of NiAl (9). Another way that structure can affect the fracture behavior of a brittle material is through texture. In ceramic materials, texture can have a significant effect on fracture toughness even when the grain size and porosity are kept constant (10, 11). Therefore, by controlling and optimizing both grain size and texture it may be possible to improve the low temperature properties of NiAl.

To date, there have been several measurements of texture in NiAl (12-18), but no systematic studies have examined the manner in which structure (both grain size and texture) evolves within wrought NiAl alloys or its corresponding fracture behavior. Consequently, the purpose of this study was to determine the manner in which structure develops in extruded NiAl, and to examine how extrusion parameters affect fracture behavior. This was accomplished by examining the effect of extrusion temperature on the grain size, texture, and room temperature fracture toughness.

## Experimental Procedures

Powder from a single lot of -20/+100 mesh prealloyed NiAl, Heat P1810, was extruded under different processing conditions. The prealloyed powder was stoichiometric and contained 0.09 at.% nitrogen. The nitrogen was present mainly in the form of fine AlN precipitates and it had no discernable effect on the mechanical properties of the material (19). Approximately 400 grams of powder was placed in each mild steel extrusion can (50 mm diameter, 140 mm long, 6 mm wall thickness). The cans were evacuated and welded airtight. Prior to extrusion the cans were placed in a furnace and allowed to soak at the desired extrusion temperature for approximately an hour. The cans were transferred in 5-10 seconds to the heated (533 K) die container of the extrusion press, and extruded through a conical die with a 16:1 area reduction and 90 degree die angle. All extrusions were made using a vertical Loewy Hydropress with a 300 ton capacity. The load-time response of the extrusion runs was autographically recorded. The extrusion process took place within 2-4 seconds. After extrusion, the steel cans were removed by pickling the extruded rods in a dilute nitric acid bath. Specimens for structural characterization, tensile and fracture toughness testing were machined from the remaining NiAl rod. Results of the tensile tests will be reported at a later date.

Selected specimens from each extrusion rod were used for microscopy and texture measurements. Both longitudinal and transverse sections were prepared. The grain size was measured after etching in a solution of 75 ml HF + 150 ml H<sub>2</sub>O + 100 gm molybdic acid. Differential interference contrast (DIC) micrographs of both sections were taken and the average grain size was measured using a circular intercept method. Samples from one extrusion, (L3010) were annealed to determine static recrystallization behavior. The specimen was heated at 8.2 K/min to 1773 K, held for 30 minutes, and cooled at 100 K/min. The same specimens were used for texture measurements. A Scintag XDS-2000 Diffractometer with a Huber ring pole figure goniometer system was used in reflection mode to measure {110}, {200}, and {211} pole figures with sample normals being parallel to the extrusion direction. All specimens were measured under the same experimental conditions. Spherical NiAl powder was used to determine the experimental defocusing correction, so that experimental pole figures are accurate representations of the textures. The data were further

processed using the popLA software package (20) using the default number of iteration steps on all runs to produce inverse pole figures from a sample orientation distribution.

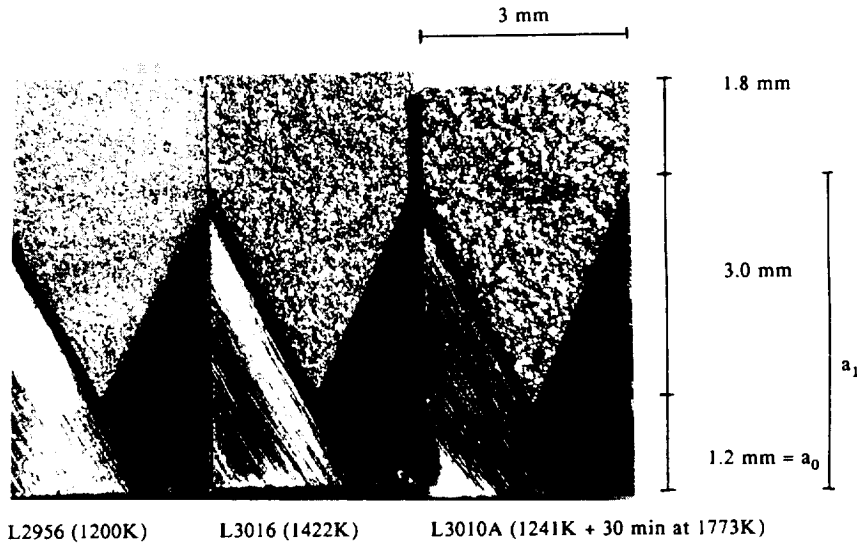


Figure 1 - Examples of three fracture surfaces, and the nominal dimensions of the chevron-notch fracture toughness specimens. The thickness of the notch was 0.2 mm.

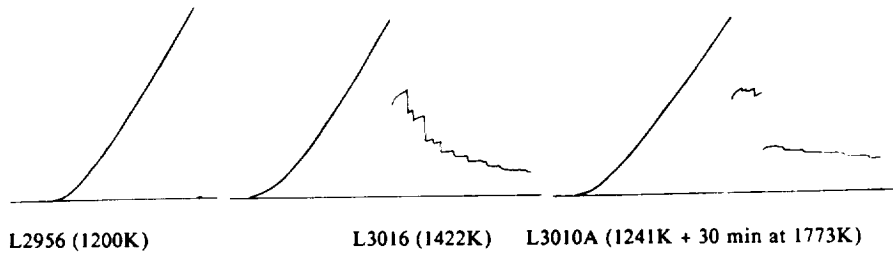


Figure 2 - Examples of load vs. time records from the three fracture toughness specimens shown in Figure 1, (a) L2956, extruded at 1200K, (b) L3016, extruded at 1422 K, and (c) L3010A, which was extruded at 1241K and annealed for 30 min at 1773 K.

Fracture toughness testing was accomplished at room temperature in accordance with ASTM E 399-81 (21) using a four point bending fixture with an inner span  $S_2$  of 20 mm and an outer span  $S_1$ , of 40 mm. The fixture and rollers were made from hot pressed alpha silicon carbide. The chevron notched specimens were nominally 50 mm long (L), 6 mm wide (W) and 3 mm thick (B) with a chevron notch of 0.2 mm width made with a thin diamond blade having the geometry shown in Figure 1. The long dimension was parallel to the extrusion direction. The samples were deformed at a constant crosshead speed of 76 nm/sec using a universal screw driven testing machine. The maximum load at fracture ( $P_{max}$ ) was between 155-222 N for every specimen. Most of the specimens exhibited a progressive failure, with the load stabilizing at lower values each time the crack arrested after the initial fracture (Figure 2). The test was stopped when the load dropped below about 20 N, and the specimen was manually separated. The fracture toughness  $K_{Ic}$  values were computed using:

$$K_{Ic} = \frac{P_{max} Y_{min}^* (S_1 - S_2)}{BW^{3/2}}$$

The compliance function  $Y^*$  was derived from the Blum slice model (22). The  $Y_{min}^*$  value was obtained by curve fitting, i.e.

$$Y_{min}^* = (3.08 + 5.0a_0 + 8.33a_{min}^2) S_1 - S_2 / Wx [1 + 0.007 (S_1 - S_2 / W^2)^0.5 (a_1 - a_0 / 1 - a_0)]$$

where all the parameters specified (Figure 1) were the actual measurements taken from each fractured specimen using an optical microscope. These specimens were designed to produce a lower stress intensity factor per unit load ( $K_I/P$ ) as the initial crack was formed, followed by a stable crack growth as the load increased. Under these conditions the  $K_I/P$  undergoes a minimum corresponding to the maximum load followed by an increase as the crack advances in an unstable way, but stable crack growth must precede the final unstable crack growth. To be a valid test, this condition would result in a nonlinear region between the initial elastic loading region and fracture on a load-displacement curve. Since the load-displacement data for the NiAl did not exhibit the stable crack growth before unstable crack propagation (as required in this technique), technically valid  $K_{Ic}$  fracture toughness values could not be computed. Instead, the critical stress intensity,  $K_Q$ , was obtained from the maximum load values.

### Results and Analysis

The extrusion parameters for all samples in this study are shown in Table I. The indicated extrusion temperatures are the temperature of the furnace prior to the extrusion. The actual temperature in the extrusion is not known, since it is affected by the transfer time and adiabatic heating (23). The breakthrough pressure of the intermetallic as it began to exit the die and the steady state running pressure at the end of the extrusion were resolvable from the pressure-time data, and are indicated. The pressures listed in Table I are higher than the operative flow stress in the NiAl due to friction and other details of the extrusion process. Two partial extrusions and one quenched extrusion were made, as indicated in Table I.

TABLE I EXTRUSION PARAMETERS

Specimen	Furnace Transfer		Breakthrough and Running Pressure, MPa		Strain Rate sec <sup>-1</sup>
	Temp., K	time, sec			
L2955	1191	4.6	190	190	2.3
L2956	1200	4.5	190	183	5.6
L3010 Partial	1241	5.0	190	190	1.15
L3011	1233	4.2	190	182	3.8
L3012 Quench	1247	5.3	190	167	5.0
L3013	1255	5.6	177	152	6.25
L3014 Partial	1311	6.0	190		
L3015	1366	5.5	185	177	4.8
L3016	1422	5.6	167	152	6.8
L3017	1505	5.3	119	91.3	7.5

### Grain Size

Optical micrographs for several of the samples are shown in Figure 3. Stringers of fine particles, resulting from the prior oxide surfaces of the powders, are evident in the larger grains. In many cases they correspond with grain boundaries, and they also surround regions dominated by smaller grains. Overall, the grain size clearly increases with extrusion temperature (Figure 4). Arrhenius plots of the transverse and longitudinal grain size data (Figure 5) result in activation energies for

grain growth of 31 and 43 kJ/mol, respectively. However, the scatter in the data at the lower temperatures resulting from regions of small grain sizes causes uncertainty in these values. In Figure 5, our data are compared with data of Haff and Schulson (24), who investigated grain growth kinetics by annealing samples taken from an ingot of Ni-49Al that was extruded at 773 K at an 8:1 reduction. When their data are extrapolated to 3.6 seconds, approximately the time it takes to extrude, good agreement between our measurements and their data is obtained. Haff and Schulson (24) calculated a grain growth activation energy of approximately 70 kJ/mol. The data of this investigation are comparable, considering the amount of scatter in our low temperature data.

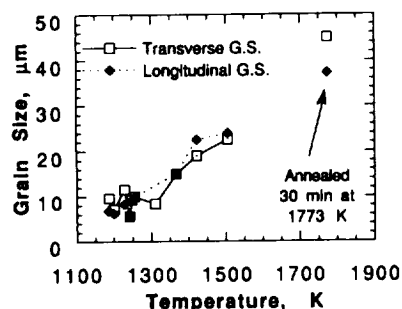


Figure 4 - Grain size increases with extrusion temperature. The sample at 1773 K is the annealed specimen partially extruded at 1241 K.

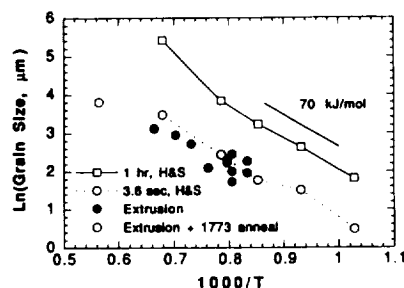


Figure 5 - Arrhenius plot of extruded grain size data compared with growth kinetics from Haff and Schulson.

### Texture

Figure 6 shows inverse pole figures for NiAl at each extrusion condition. With increasing extrusion temperature, the population of grain orientations changes from a  $\langle 110 \rangle$  fiber texture to a  $\langle 111 \rangle$  texture. Figure 7 shows intensities of several orientations plotted versus temperature, and it is evident that  $\langle 111 \rangle$  orientations grow at the expense of  $\langle 110 \rangle$  orientations with increasing temperature, while no other components of texture change significantly. The data that deviate the most from the trend represent partial extrusions. Figure 8 shows directly that fine grained, low temperature extrusions possess a strong  $\langle 110 \rangle$  extrusion texture. The specimen with the smallest grain size, L3010, was a partial extrusion with a strong  $\langle 110 \rangle$  texture, and upon static annealing, it developed a strong  $\langle 111 \rangle$  texture. As the extrusion temperature is increased, more grain growth occurs which results in the  $\langle 111 \rangle$  texture. A close inspection of the data near the  $\langle 111 \rangle$  poles indicates that intensity at  $\langle 111 \rangle$  is always a local minimum. Higher intensities were found about  $5^\circ$  from the  $\langle 111 \rangle$  orientation, and the highest intensities were near  $\langle 556 \rangle$  (Figure 9). The  $\langle 111 \rangle$  intensities were averaged with orientations  $5^\circ$  away from  $\langle 111 \rangle$  for the plots in Figures 7 and 8.

A qualitative analysis of texture evolution was made using a comparison between measurements and Schmid factors of potential slip systems in NiAl. The von Mises criterion for an arbitrary shape change requires five independent slip systems to operate in any grain. Table II shows the largest Schmid factors for several possible slip systems in NiAl at the important crystal orientations. The probability for slip in a grain with a given orientation is high when the resolved shear stress on one of its slip systems is high, which corresponds with a high Schmid factor. The maximum value of the Schmid factor is 0.5, which occurs when a slip system has both its plane normal and slip direction oriented  $45^\circ$  from the deformation axis. Since 5 slip systems are needed for an arbitrary shape change, grains with slip systems having a high average Schmid factor will contribute more strain to the system, assuming the grain remains in the same orientation.

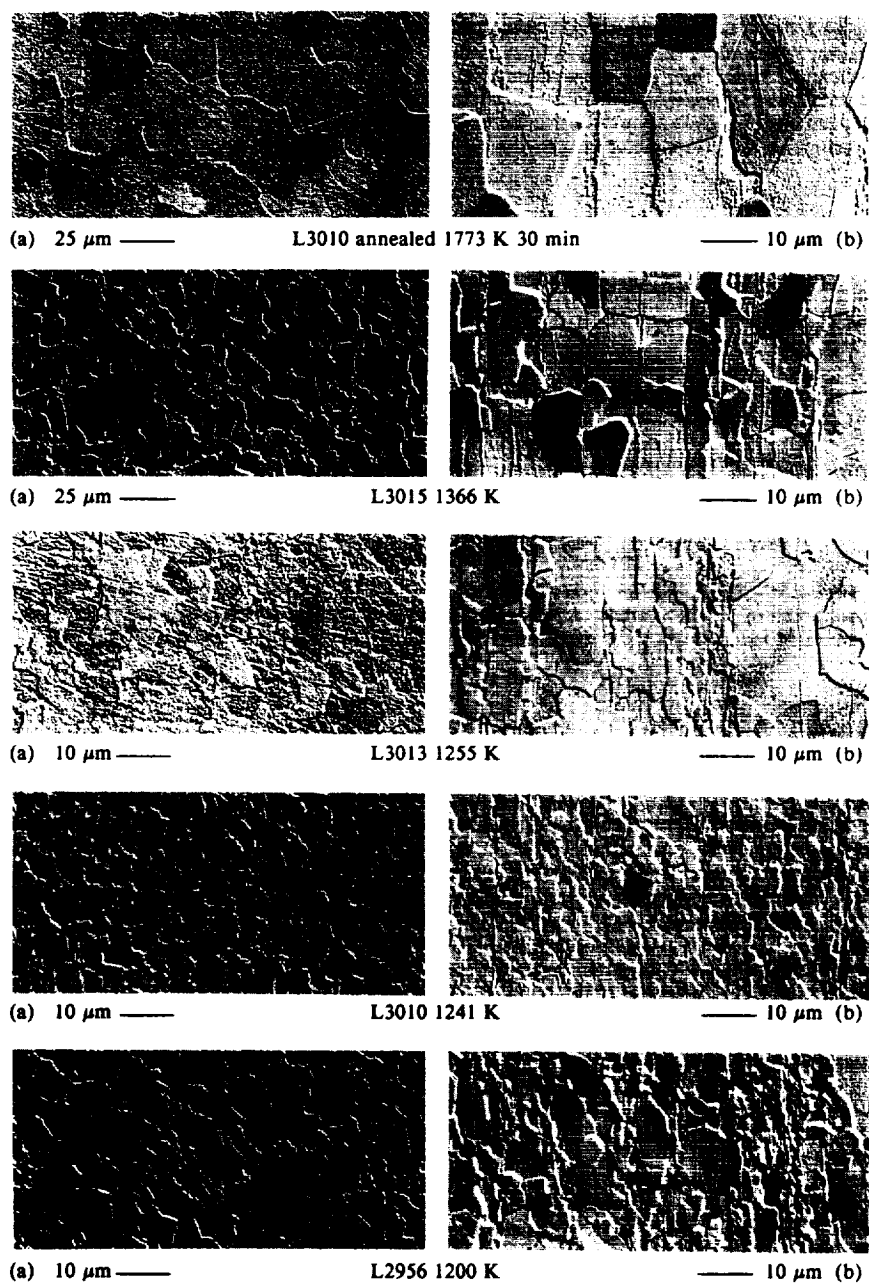


Figure 3 - Micrographs of the microstructure for several specimens;  
(a) transverse sections and (b) longitudinal sections.

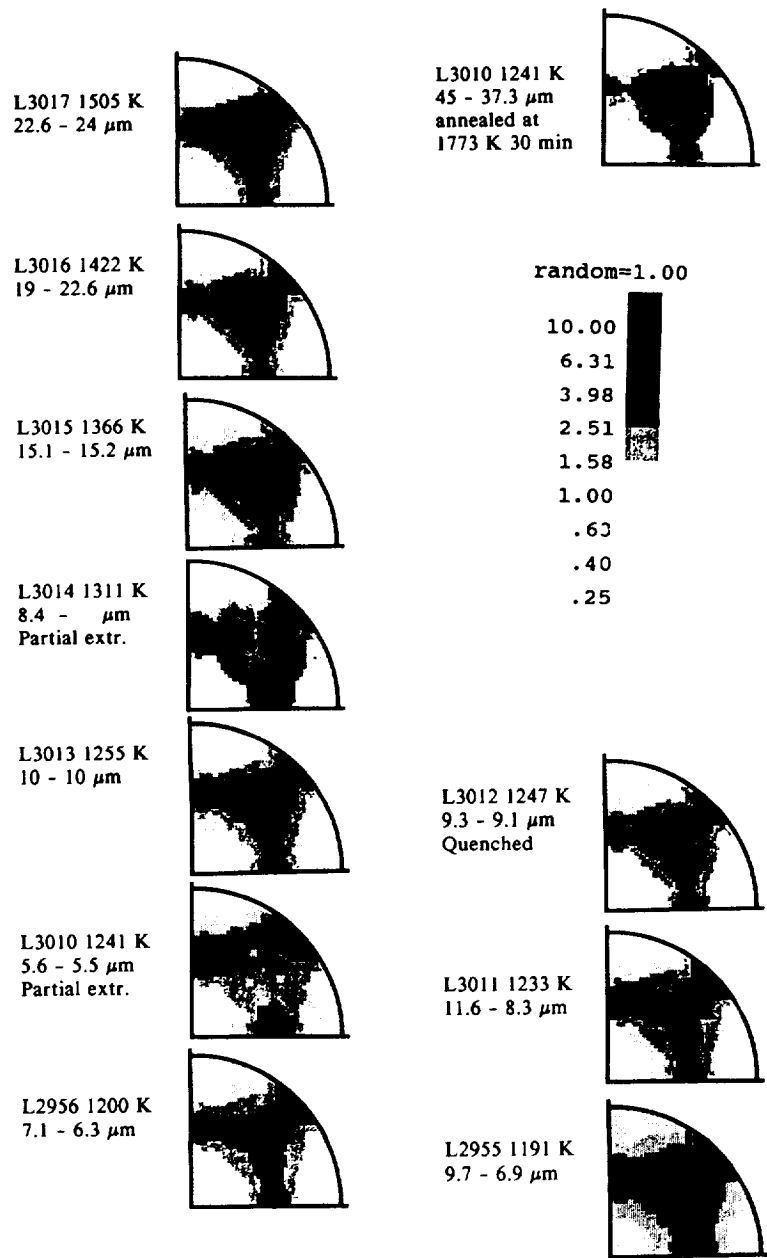


Figure 6 - Inverse pole figures are shown with approximate extrusion temperatures and grain size (first value is longitudinal, second is transverse measurement).

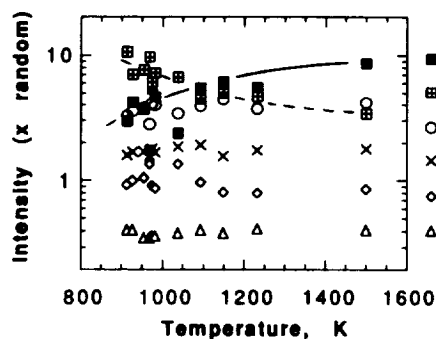


Figure 7 - Inverse pole figure intensities vs. extrusion temperature for several orientations on the perimeter of the stereographic triangle.

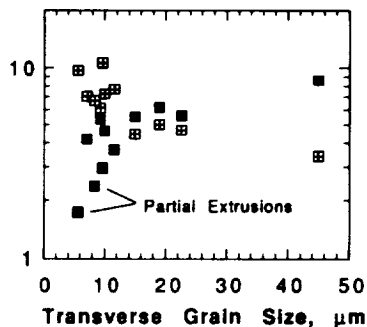


Figure 8 - Inverse pole figure intensities vs. grain size.

TABLE II  
SCHMID FACTORS FOR POTENTIAL SLIP SYSTEMS IN IMPORTANT ORIENTATIONS

Slip System	Crystal Direction in [001]-[111]-[101] Stereographic Triangle										
	[223]	[556]	[111]	[656]	[323]	[212]	[313]	[616]	[101]	[506]	[203]
"normal"											
{110}<100>	.50*1 .42*2	.49*1 .45*2	.47*3 0	.48*2 .44*1	.48*2 .39*1	.47*2 .31*1	.44-2 .22*3	.41-2 .29-2	.35-4 0	.35-4 0	.33-4 0
"cube"								.12*1			
{100}<100>	.35-4 .26-2	.35-4 .29-2	.33-6 0	.37-2 .31-4	.41-2 .27-4	.44-2 .22-4	.47*2 .16-4	.49*2 .08-4	.50*2 0	.49*2 0	.46*2 0
{112}<111>	.37*2 .25-2	.35*2 .20-2	.31*3 .16-6	.37*1 .28-1	.43*1 .24-2	.47*1 .26-1	.50*1 .35-1	.50*1 .42-1	.47*2 .24-4	.47*2 .30-2	.45*2 .36-2
"bcc, fcc"											
{110}<111>	.36-2	.31-2	.27-6	.32*2	.37*2	.41*2	.43*2	.43*2	.41*4	.44*2	.47*2
{111}<110>	.29-2	.29-2		.25-2	.22-2	.23-2	.30-2	.36-2	0	.37-2	.31-2
{110}<110>	.15-4	.06-4	0	.06-4	.11-4	.17-4	.21-4	.24-4	.25-4	.30-2	.35-2
Average Schmid Factor; local maxima are bold (accurate to 3 digits):											
* Highest 5	.416	.417	.408	.419	.430	.417	.419	.406	.470	.472	.464
† <100> x 2	.426	.436	.432	.437	.438	.412	.409	.392	.479	.478	.463
‡ no <100>	.374	.345	.314	.349	.400	.440	.463	.464	.450	.459	.465

The number following - or \* is the number of slip systems with the same Schmid factor.

\* After the top 3 <100> directions are used, the next two highest <111> or <110> directions are used in the average.

† <100> slip systems are weighted 4 times more than <111> slip systems.

‡ Average of Schmid factors for non-<100> slip systems.



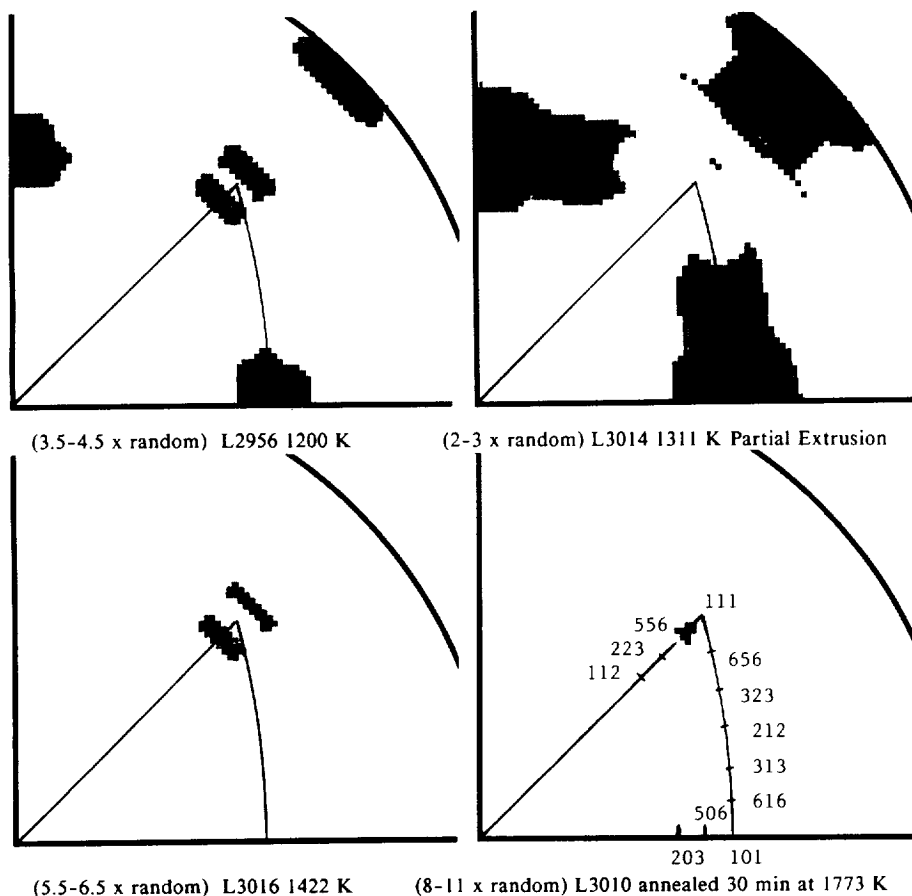


Figure 9 - Examples of  $\langle 111 \rangle$  regions in a finely defined scale indicate that intensities at  $\langle 111 \rangle$  are actually local minima. The scale is altered in each case to show this effect.

In an attempt to estimate probable slip systems operating at the important orientations, the following strategy was used to identify the 5 most probable slip systems. Since  $\langle 100 \rangle$  slip has the lowest resolved shear stress, the three independent  $\langle 100 \rangle$  slip directions with the highest Schmid Factor are chosen, followed by the next two highest Schmid factors for  $\langle 110 \rangle$  or  $\langle 111 \rangle$  slip directions. These five slip systems are noted by a \*, and averaged. Since the resolved shear stress for  $\langle 100 \rangle$  slip is lower than for  $\langle 111 \rangle$  or  $\langle 110 \rangle$  slip, the weighted average marked by † gives preference to  $\langle 100 \rangle$  slip by a factor of two. The two averages are not much different, but the weighted average gives a variation in average Schmid factor that corresponds with the local intensities in the inverse pole figures in Figures 6 and 9. The average of non- $\langle 100 \rangle$  slip systems is also computed in average ‡, which shows that the average Schmid factor for these non- $\langle 100 \rangle$  slip systems is at a maximum near the  $\langle 110 \rangle$  orientation.

A grain in a  $\langle 110 \rangle$  orientation has only two possible  $\langle 100 \rangle$  slip systems, but they have the highest possible resolved shear stress on a  $\{100\}$  plane (the third  $\langle 100 \rangle$  direction is  $90^\circ$  from the deformation axis has no resolved shear stress). Since the  $\langle 100 \rangle$  slip system will not cause grain rotations, no texture can evolve from this slip system alone (18). Therefore the three other slip systems that operate must be responsible for stabilizing the  $\langle 110 \rangle$  orientation. Two  $\{112\}\langle 111 \rangle$  slip directions

have a high Schmid factor (0.47), and there are a choice of many equivalent  $\{110\}\langle 111 \rangle$  or  $\{111\}\langle 110 \rangle$  slip directions to provide the fifth slip system. Since  $\langle 111 \rangle$  or  $\langle 110 \rangle$  slip requires a much higher stress (25), deformation on these systems will be minimal; only the slip needed for compatibility will occur on these slip systems.

The origin of the  $\langle 111 \rangle$  texture is considered next, since the reason for this being the nucleating orientation of the recrystallization texture has not been established. Though the  $\langle 110 \rangle$  orientation appears to be a "deformation" texture, near- $\langle 111 \rangle$  orientations are also apparent in extrusions at low temperature where grain growth is inhibited (L2956 in Figures 6,9). We hypothesize that it results from a "metastable" minority deformation texture component that has a grain growth advantage due to having high angle boundaries with the dominant  $\langle 110 \rangle$  textured neighboring grains. From Table II, it is apparent that the slip system situation is complicated near the  $\langle 111 \rangle$  orientation: The maximum resolved shear stress for the normal  $\{110\}\langle 100 \rangle$  slip system is at  $\langle 322 \rangle$ , about  $10^\circ$  from the  $\langle 111 \rangle$  orientation. Comparing the highest five Schmid factors in Table II for orientations near  $\langle 111 \rangle$ , a  $\{112\}\langle 111 \rangle$  slip system will probably be active. The next highest Schmid factor is in the "bcc, fcc" system. However the maximum Schmid factor in the  $\{112\}\langle 111 \rangle$  and  $\{110\}\langle 111 \rangle$  systems have the same  $\langle 111 \rangle$  vector; if these are not independent slip systems, then the one of the "fcc"  $\{111\}\langle 110 \rangle$  slip systems has a high Schmid factor for  $\langle 110 \rangle$  slip. Since fcc and bcc single crystals rotate in tension in opposing directions toward  $\langle 111 \rangle$  and  $\langle 110 \rangle$  orientations respectively (26), the metastability may be maintained if the two non- $\langle 100 \rangle$  slip systems have a  $\langle 110 \rangle$  and a  $\langle 111 \rangle$  vector. These two slip vectors may counter balance each other so as to preclude large rotations.

#### Fracture Toughness:

Figure 10 shows the plot of the critical stress intensity  $K_{Ic}$  vs. grain size. There is not a large effect of extrusion temperature or grain size on toughness when all the data are considered. The toughness values varied between 6 and 10  $\text{MPa}\sqrt{\text{m}}$  with an average of  $7.6 \pm 1 \text{ MPa}\sqrt{\text{m}}$ . A statistical analysis of variations suggested that the toughness increased linearly with grain size up to 15 microns but was constant for larger grain sizes.

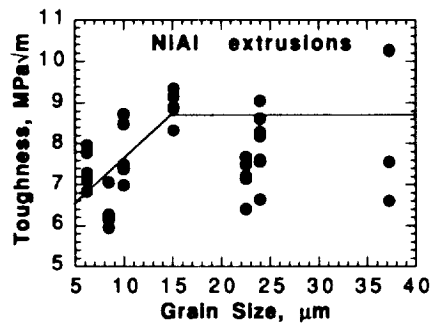


Figure 10 - The critical stress intensity  $K_{Ic}$  is between 6 and 10  $\text{MPa}\sqrt{\text{m}}$ .  $K_{Ic}$  increases slightly with grain size (and extrusion temperature).

Though some samples broke catastrophically into two distinct pieces at  $P_{max}$ , most of the specimens exhibited some residual toughness (Figure 2). The specimens that broke into two pieces after the initial fracture were from the lowest temperatures extrusions. The specimens with residual toughness exhibited a load drop but then reloaded before the next fracture event occurred. In some samples this repeated fracture and reloading occurred many times before the experiment was stopped. Two methods were used to evaluate this residual toughness. In Figure 11 the load remaining after the first fracture event is plotted versus fracture toughness. This plot shows that the load following initial fracture at  $P_{max}$  increased with increasing extrusion temperature. For a given extrusion temperature the load remaining after initial fracture at  $P_{max}$  was lower at higher  $K_{Ic}$  values, since the higher load at fracture represented more stored elastic energy in the specimen. Figure 12 shows that the number of times the specimen reloaded before reaching an arbitrary low load also increased with extrusion temperature. From these observations, it appears that the lowest temperature extrusions exhibited a constant or accelerating crack velocity, but the majority of the specimens exhibited deceleration and arrest behavior after initial fracture.

SEM observations of the fracture surfaces indicated that at least 2/3 of the fracture area consisted of cleavage type separation. Figure 13 suggests that initiation of the fracture occurred in an intergranular manner, but after the crack propagated through a few grain boundaries, cleavage fracture became dominant. In many instances, a cleavage crack changed its plane slightly as the

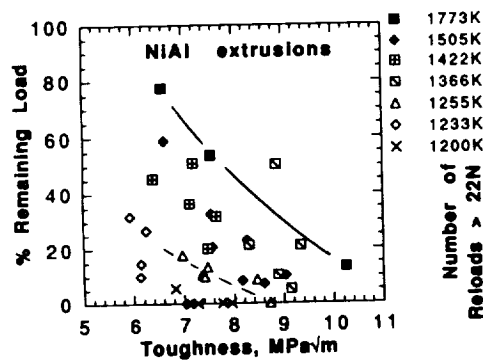


Figure 11 - The fraction of the fracture load remaining after initial fracture decreases with toughness, and increases with extrusion or annealing temperature.

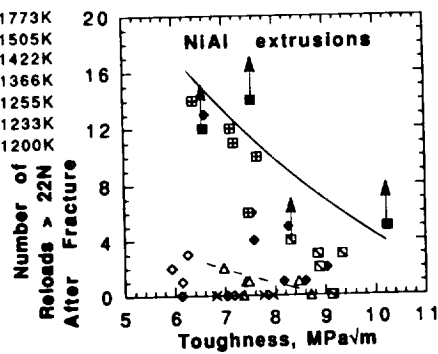


Figure 12 - The number of reloads greater than 22 N (5 lb) increases with extrusion temperature. Specimens with arrows were terminated before reaching the 22 N load.

fracture moved from one grain to another (e.g. L3016, L3010A in Figure 13). Samples L3016 and L3010A, had a rougher surface than L2956 due to the larger grain size. These two specimens also exhibited an increase in surface roughness as the crack entered the top rectangular part of the specimen (Figure 2). The greater roughness on the fracture surface correlates with reloading after initial fracture, and the reloading appears to have taken place when the crack was in the top rectangular part of the specimen. In areas with larger topological discontinuities, a cleavage fracture region was apparently halted by a change in mode to intergranular fracture, which diverted the crack by a distance of a couple grains (Figures 13-14). Thereafter, the crack switched back to a cleavage fracture mode. On the other hand, specimen L2956 (extruded at 1200K) had a very smooth appearance across the entire fracture surface, except for a few ridges parallel to the crack growth direction about 50  $\mu\text{m}$  above the fracture tip (Figure 13). In this specimen there was more surface roughness in the chevron notch region than in the top rectangular part of the specimen, where the area fraction of cleavage was 80-90% and river lines dominated the cleavage surfaces.

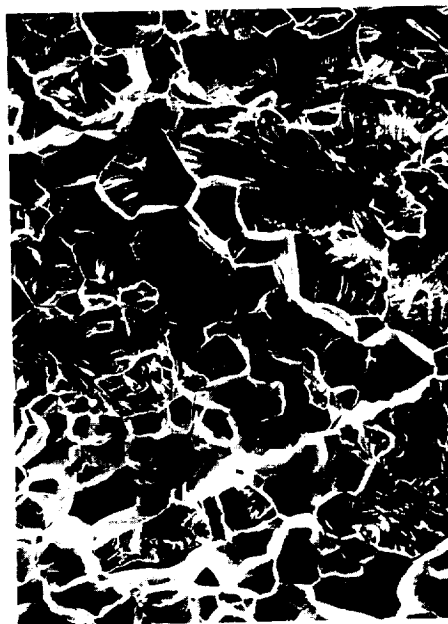


Figure 14 - Example of a crack arrest region in the rectangular part of L3010A. The crack arrested in the lower portion, and crack grew perpendicular to fracture plane to find new cleavage site. The crack grew in the upward direction.



20  $\mu\text{m}$  —  
L2956 1200 K



L3010 50  $\mu\text{m}$  —  
annealed 1773 K 30 min



20  $\mu\text{m}$  —  
L3016 1422 K

Figure 13 - SEM micrographs indicate that fracture started from intergranular separation, but within a few grains, cleavage fracture became the dominant mode of separation.

## Discussion

### Microstructure and Texture

The texture and grain growth observations are consistent with results in the literature (12-18). Most of the reported textures exhibit  $\langle 111 \rangle$  texture, since they were extruded at the higher temperature range used in this study. Dymek et. al. compared extrusion textures in a cast plus extruded binary NiAl alloy and a mechanically alloyed Ni-45Al. Both were extruded at 1400 K in a 16:1 reduction ratio (15,16). Their extruded ingot exhibited an equiaxed 30  $\mu\text{m}$  grain size with  $\langle 111 \rangle + \langle 313 \rangle$  texture. Their description of the  $\langle 111 \rangle$  texture as a discontinuous recrystallization texture is consistent with the static annealing result of this study. The MA material had submicron grains, and it exhibited a  $\langle 110 \rangle$  texture. This texture was ascribed to a bcc kind of deformation texture that was preserved by the boundary pinning effect of the fine particles that resulted from the mechanical alloying process.

The  $\langle 110 \rangle$  texture has been ascribed to "bcc"-like slip processes (13,15,16,18). This is problematic, since it implies that  $\langle 111 \rangle$  slip controls grain rotation. Post mortem TEM studies indicate that the majority of dislocations observed after hot deformation of NiAl are of the  $\langle 100 \rangle$  type, and  $\langle 110 \rangle$  and  $\langle 111 \rangle$  dislocation segments have only occasionally been observed (5, 27-29). However, if  $\langle 110 \rangle$  and  $\langle 111 \rangle$  dislocations were operative during the extrusion process, they could not be expected to survive cool-down following extrusion, since their line energy is much higher than  $\langle 100 \rangle$  dislocations (25), and recovery will promote decomposition to minimize the line energy. Changes in core structure to form  $\langle 100 \rangle$  dislocations are probable since both  $\langle 110 \rangle$  and especially  $\langle 111 \rangle$  dislocations are unstable in NiAl at intermediate temperatures (30,31). An increase in line length that reduces line energy from considerations such as these has been observed and modeled (32).

A study by Margevicius and Cotton (18) of the textures resulting from hot compression tests near the brittle to ductile transition temperature (BDTT) (773-998 K) have shown that the texture components do not change appreciably even after 75% strains. They determined that only a combination of glide and climb of  $\langle 100 \rangle$  dislocations could explain this lack of grain rotations, and showed that  $\langle 100 \rangle$  slip alone will not cause any rotations. However, in a hydrostatic extrusion at 573 K, below the BDTT (9), a sharp  $\langle 110 \rangle$  texture was obtained in a condition where minimal diffusion is expected. This indicates that rotations and formation of a deformation texture can only be achieved in conditions with a large hydrostatic stress. Therefore the presence of  $\langle 110 \rangle$  textures at high temperature can be ascribed to a deformation texture process. This strongly suggests  $\langle 111 \rangle$  slip, but slip in this direction requires a resolved shear stress several times higher than for  $\langle 100 \rangle$  slip. This is possible in extrusion conditions since typical extrusion pressures are several times the yield stress of the extruded material (33), due to friction, adiabatic heating, and geometric details of the extrusion process. Also, in a study of large rolling reductions in NiAl, textures similar to those obtained in cold rolled low carbon steels were obtained (17). Thus,  $\langle 111 \rangle$  slip is probable in these rolling conditions as well, due to the hydrostatic stress component imposed between the rolls. Since climb is possible even at the BDTT, there is opportunity for the high energy  $\langle 111 \rangle$  or  $\langle 110 \rangle$  dislocations to decompose or disappear during the cooldown immediately following extrusion.

The quenched partial extrusions of this study had the smallest grain sizes and a strong  $\langle 110 \rangle$  texture, but also significant near- $\langle 111 \rangle$  components. The change in texture upon annealing to  $\langle 111 \rangle$  shows that either new orientations had already been nucleated, or that they were "metastable" during deformation. The analysis above shows that the stability of the near- $\langle 111 \rangle$  component is difficult to assess. Also, the role of climb has been ignored in the analysis. However, there are high Schmid factors for both  $\langle 100 \rangle$  and other slip systems for grains oriented at  $\langle 110 \rangle$  and  $\langle 111 \rangle$  orientations, so slip activity will be greater in these grains than in others. Consequently it is probable that there will be more stored strain energy in these orientations compared to others, and this suggests that these are the prime locations for nucleation of new grains. Since the  $\langle 111 \rangle$  orientation is 35° from the dominant  $\langle 110 \rangle$  deformation component,  $\langle 111 \rangle$  grains satisfy the requirement of a large angle mismatch to provide rapid boundary mobility for primary recrystallization.

### Room Temperature Fracture Toughness:

The fracture toughness for binary polycrystalline NiAl is usually reported to be between 5 and 6 MPa $\sqrt{m}$  (34-36). Toughness testing of cast plus extruded binary NiAl using the same sample geometry and testing conditions as in this study also provided fracture toughness values between 5 and 6 MPa $\sqrt{m}$  (37). With an average fracture toughness of 7.6 MPa $\sqrt{m}$ , the material in this study is roughly 35% tougher than other binary NiAl alloys, though it should be noted that toughness has not been previously determined for a powder extruded alloy. This difference in toughness is still under investigation. However, it is suspected that the significantly lower carbon level and/or the higher residual dislocation density observed in this powder extruded material (19) may contribute to the higher toughness, since this alloy would be less affected by strain aging embrittlement effects such as those observed by Hack et. al. (38) in single crystal NiAl.

Fracture studies in NiAl single crystals indicate that toughness depends upon crystal orientation (39, 40). For single crystals loaded to promote cracks on {110} planes, the fracture toughness was low, from 4 to 6.4 MPa $\sqrt{m}$  (39). Crystals oriented to cause fracture on {100} planes exhibited twice the toughness, at 8-12 MPa $\sqrt{m}$  (39, 40). Cleavage energies have been computed for {100} and {110} planes, and {110} planes have a 30% lower energy, which is consistent with the observed fracture toughness values (41).

In the <111> textured specimens with larger grain sizes, cleavage also dominated the fracture surface, but the cleavage surfaces were less flat, showing numerous river line striations. The slightly higher toughness observed is consistent with a greater amount of energy being required for cleavage on higher energy planes. The residual toughness is attributed to cleavage arrest and conversion to intergranular separation out of the fracture plane (Figure 14), which is most evident in the top rectangular part of the specimen. In this case, the grain orientations next to the arrest are of interest, as they apparently did not have an orientation that could easily propagate the cleavage fracture in the advancing crack.

On the other hand, it could also be argued that the increase in toughness is due to extrinsic effects, such as a larger grain size, and unrelated to texture. Inspection of the fracture surfaces demonstrates that the planarity of the fracture surfaces decreases with increasing grain size. When intergranular separation diverts the fracture, the diversion is larger when the grain size is larger. The fact that the cleavage fracture of the small grains in the <110> textured sample did not occur in a continuous manner across all grains indicates that grain boundaries can deflect cleavage cracks even when the grains are oriented for easy cleavage. Clarification of this issue could be obtained by obtaining <111> textured specimens with a small grain size, and <110> textured samples with a large grain size, but the processing needed to obtain this is not obvious. However, the major point to be obtained from the present work is that while there may be subtle effects, neither grain size or texture have an overwhelming influence on the fracture toughness of NiAl.

### Conclusions

1. Extrusion temperatures affect texture, with <110> fiber texture being evident at lower temperatures and <111> fiber texture being evident at higher temperatures. The <110> texture is a deformation texture stabilized by <111> slip. The <111> texture arises from a grain growth recrystallization where minority populations of <111> orientations have large angle boundaries that have high mobility.
2. Fracture toughness in powder processed NiAl varies from 5.5 to 9 MPa $\sqrt{m}$ . As the texture changes from <110> to <111> the grain size gets larger. The slight increase in toughness with grain size can be attributed to extrinsic crack deflection effects, and also due to a reduction of grain orientations oriented for easy cleavage on <110> planes.
3. Neither grain size or texture have a strong effect on fracture toughness of NiAl.

## References

1. R.R. Bowman and R.D. Noebe: in Superalloys 1992, S.D. Antolovich et. al., The Minerals, Metals & Materials Society, Warrendale, PA., 1992, pp. 341-352.
2. R.D. Noebe, F.J. Ritzert, A. Misra and R. Gibala: NASA TM 103796, 1991.
3. E.P. George and C.T. Liu, *J. Mater. Res.*, **5**, 1990, 754-762.
4. R.D. Noebe and M.K. Behbehani, *Scripta Metall. Mater.*, **27**, 1992, 1795-1800.
5. J.D. Cotton, R.D. Noebe and M.J. Kaufman, *Intermetallics*, **1**, 1993, 117-126.
6. R.D. Noebe, R.R. Bowman, and M.V. Nathal, *Int. Mater. Revs.*, **38**, 1993, 193-232.
7. K.H. Schwalbe, *Eng. Fract. Mech.*, **9**, 1977, 795-832.
8. E.M. Schulson, *Res. Mech. Lett.*, **1**, 1981, 111-114.
9. R.D. Noebe, R.R. Bowman, C.L. Cullers and S.V. Raj: in High Temperature Ordered Intermetallic Alloys IV, ed. L. Johnson et. al., Mat. Res. Soc. Symp. Proc. Vol. 213, 1991, pp. 589-596.
10. R.W. Davidge: in Proceedings of the British Ceramic Society, No. 20, June 1972, British Cer. Soc., Stoke-on-Trent, England, pp. 364-378.
11. M. McNamee and R. Morrell: in Proceedings of the 12th International Conference on Science of Ceramics, Faenza, Italy, 1984, pp. 629-634.
12. R.W. Margevicius and J.J. Lewandowski, *Scripta Metall. Mater.*, **29**, 1993, 1651.
13. T.R. Bieler, R.D. Noebe, J.D. Whittenberger, and M.J. Luton: in Intermetallic Matrix Composites II, ed. D.B. Miracle, D.L. Anton, J.A. Graves, MRS Symp. Proc. Vol. 273, 1991, pp. 165-170.
14. P.S. Khadkikar, G.M. Michal and K. Vedula, *Metall. Trans.* **21A**, 1990, 279.
15. S. Dymek, S.H. Hwang, M. Dollar, J.S. Kallend, P. Nash, *Scripta Metall. Mater.*, **27**, 1992, 161-6.
16. M. Dollar, S. Dymek, S.J. Hwang, and P. Nash, *Metall. Trans.*, **24A**, 1993, 1993-2000.
17. K.J. Bowman, J. Jenny, S. Kim, and R.D. Noebe, *Mater. Sci. Eng.*, **A160**, (1993), 201-8.
18. J.D. Cotton and R.W. Margevicius: submitted to *Acta Metall. Mater.*, 1993.
19. R.D. Noebe and A. Garg, submitted to *Scripta Metall. Mater.*, 1993.
20. J.S. Kallend, U.F. Kocks A.D. Rollett and H.-R. Wenk, *Mat. Sci. Eng.*, **A132**, 1991, 1.
21. ASTM E 399-83, Annual Book of ASTM Standards, Vol. 3.01, ASTM, Philadelphia, PA., 1988, pp. 477-504.
22. J.I. Blum, *Eng. Fract. Mech.*, **7**[3], 1975, 593-604.
23. C.M. Sellars, *Mat. Sci. Tech.*, **1**, 1985, 325.
24. G.R. Haff and E.M. Schulson, *Metall. Trans.*, **13A**, 1982, 1563-1566.
25. D.B. Miracle, *Acta Metall. Mater.*, **41**, 1993, 649-684.
26. W.A. Backofen, Deformation Processing, Addison-Wesley Publishing Company, Reading, MA., (1972).
27. I. Baker and E.M. Schulson, *Metall. Trans.*, **15A**, 1984, 1129-1136.
28. C.H. Lloyd and M.H. Loretto, *Phys. Status Solidi.*, **39**, 1970, 163-170.
29. P.R. Munroe and I. Baker, *Scripta Metall.*, **23**, 1989, 495-499.
30. J.T. Kim and R. Gibala: in High Temperature Ordered Intermetallic Alloys IV, ed. L. Johnson et. al., Mat. Res. Soc. Symp. Proc. Vol. 213, 1991, pp. 261-266.
31. J.T. Kim: Ph.D. Thesis, The University of Michigan, Ann Arbor, MI., 1990.
32. U. Glatzel, K.R. Forebes and W.D. Nix, *Phil Mag.*, in press
33. A. Greasley and H.Y. Shi, *Mat. Sci and Tech.* **9**, 1993, 42-47.
34. K.S. Kumar, S.K. Mannan and R.K. Viswanadham, *Acta Metall. Mater.*, **40**, 1992, 1201-1222.
35. J.D. Rigney, P.S. Khadkikar, J.J. Lewandowski, and K. Vedula: in High Temperature Ordered Intermetallic Alloys III, ed. C.T. Liu et. al., MRS Symp. Proc. Vol. 133, 1989, pp. 603-8.
36. S. Reuss and H. Vehoff, *Scripta Metall. Mater.*, **24**, 1991, 65-73.
37. M. Hebsur and R.D. Noebe: unpublished data, NASA LeRC, 1993.
38. J.E. Hack, J.M. Brzeski and R. Darolia, *Scripta Metall. Mater.*, **27**, 1993, 1259-1263.
39. H. Vehoff: in High Temperature Ordered Intermetallic Alloys V, ed. I. Baker et. al., Mat. Res. Soc. Symp. Proc. Vol. 288, 1993, pp. 71-82.
40. K.M. Chang, R. Darolia, H.A. Lipsitt, *Acta Metall. Mater.*, **40**, 1992, 2727-2737.
41. M.H. Yoo and C.L. Fu, *Scripta Metall. Mater.*, **25**, 1991, 2345-2350.

